DIRECT NUMERICAL SIMULATION OF VORTEX DYNAMICS ASSOCIATED WITH A SEPARATION BUBBLE ON A ROUNDED EDGE

Eric Lamballais
Laboratoire d'Etudes Aérodynamiques UMR 6609,
Université de Poitiers, ENSMA, CNRS
Téléport 2 - Bd. Marie et Pierre Curie B.P. 30179
86962 Futuroscope Chasseneuil Cedex, France
lamballais@univ-poitiers.fr

Jorge Silvestrini
Faculdade de Engenharia,
Pontifícia Universidade Católica do Rio Grande do Sul
Av. Ipiranga 6681, 90619-900 Porto Alegre - RS, Brasil
jorgehs@pucrs.br

Sylvain Laizet
Institute for Mathematical Sciences and Department of Aeronautics,
Imperial College London
53 Princes Gate, Exhibition Road,
South Kensington Campus, London SW7 2PG, UK
s.laizet@imperial.ac.uk

ABSTRACT

The formation of a separation bubble over a generic half-body with a rounded edge is studied by DNS. Front edge curvature and body aspect ratio effects are considered by focusing on the vortex dynamics associated with the breakdown of the bubble through 3D processes. Qualitative and quantitative comparisons with previous experiments are presented. The main influences of curvature and aspect ratio are consistently recovered in present simulations. The structure of the separation bubble is in agreement with experiments, especially the combination of singular points associated with the surface flow. Behind the separated region, the examination of the mean flow reveals the presence of a pair of longitudinal counter-rotating vortices pumping fluid from the side of the body to the top of the flow. The analysis of instantaneous visualisations shows the formation of strong lambda vortices for small aspect ratios that causes ejection of the fluid through a periodic bursting process that seems to be linked to the flapping of the separation bubble. The increase of the curvature of the rounded front edge is found to increase the separation angle, in qualitative agreement with experiments, with a global growing of the size of the separation bubble in longitudinal and vertical directions. Strong curvature also tends to reduce drastically the sensitivity of the flow to upstream conditions, suggesting the occurrence of phenomena that could be interpreted in terms of convective/absolute stability.

INTRODUCTION

Most of bluff bodies (like cars, trains or buildings) have rounded edges that lead to regions where the flow is separated and reattached. The formation of separation bubbles causes the presence of eddying wakes in near-body region of the flow. The unsteady nature of the resulting vortex dynamics is of practical importance in many applications where noise emissions or structure vibrations have to be reduced through a passive or active control. Separation bubbles can be triggered by adverse pressure gradients or by curvature effects of the wall geometry. In this work, we are interested by the latter type of effects that remains significantly less studied than the former. Moreover, because most of separation bubbles are 3D in practical flow geometries [8], it is worth considering the influence of the aspect ratio of the body in cross directions. Consequently, our goal is to better understand how the combined effects of curvature and aspect ratio can select a different dynamics in the separation bubble zone as well as further downstream behind the reattached region. For this purpose, several flow configurations, already studied experimentally, are reproduced here by direct numerical simulation (DNS) and analysed by focusing on the role played by the various vortical structures involved in the dynamical changes that are observed.

FLOW CONFIGURATION AND NUMERICAL METHODS

Measurements (visualization, PIV, hot-film) have been conducted by [3, 2, 4] for a constant flow (of velocity U_∞) over a generic bluff body with different front edge radii and cross frontal sections. The model geometry and its parameters R, H_s (deduced from H), L and l are presented in figure 1. Using a low-speed water tunnel, [3, 2, 4] have considered flow regimes at moderate Reynolds numbers ($O(10^3) < Re = u_\infty H_s/\nu < O(10^4)$) so that a comparative work using DNS can be performed. For this purpose, we use a numerical code, "Incompact3d", based on sixth-order compact schemes to solve the incompressible Navier-Stokes equations. The modelling of the body is performed by an Immersed Boundary Method (IBM). Following the procedure proposed by [6], the present IBM is a direct forcing approach that ensures the no-slip boundary condition at

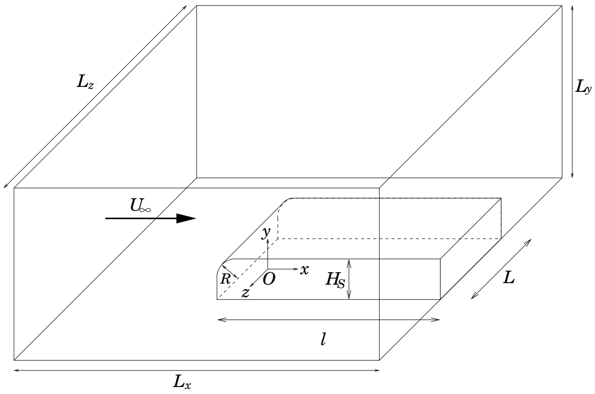

Figure 1: Schematic view of the flow configuration.

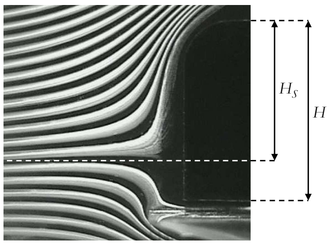

Figure 2: Relation between the height of the half-body H considered by [3, 2, 4] and its corrected value H_s used in present DNS (stagnation point located in the lower horizontal boundary of the computational domain $y = 0$).

the wall while creating artificially a flow inside the body. This internal flow, without physical significance, allows a better regularity of the velocity field across the immersed boundary, this property being of primary importance when numerical schemes of spectral or quasi-spectral accuracy are used. Combined with a sixth-order compact filtering of the convective terms, this specific IBM leads to a reduction of wiggles in the neighbourhood of the body while allowing better quantitative predictions at marginal resolution (see [6] for more details).

To be as close as possible from the experimental arrangement, only the part of the flow above the horizontal plane (x, z) including the stagnation point is considered in the simulation while the cross section of the computational domain fits exactly the experimental one. Using the location of the stagnation point reported by [3, 2, 4], the height of the half-body considered in present DNS is $H_s = 0,82H$ (see figure 2) while its length is $l = 12H_s$. The computational domain $L_x \times L_y \times L_z = 20H_s \times 5H_s \times 12H_s$ is discretized on a Cartesian grid (stretched in y) of $n_x \times n_y \times n_z = 601 \times 151 \times 401$ points. The pressure grid is staggered from the velocity grid to avoid spurious pressure oscillations. Boundary conditions are inflow/outflow in x and free-slip in y and z.

For this study, only the case $Re = 1250$ is addressed numerically. Our aim is to investigate the influence of the aspect ratio $\Lambda = L/H$ and the non-dimensional rounded edge radius $\eta = R/H$ by considering the cases $\Lambda = 2.2, 4.4, 8.8$ and $\eta = 0.8, 0.4$, these specific flow configurations being well referenced in the database of [3, 2, 4]. Note that to make easier comparisons with these experiments, we use the same definitions of Λ and η which are based on H instead of H_s. To better identify the specific 3D effects associated with the moderate values of the aspect ratios, the case $\Lambda \to \infty$ is also considered using $L = L_z$ and $n_z = 400$ while the free-slip boundary condition is replaced by a periodic one in z-direction, this limit case corresponding to the body configuration considered by [9] using LES.

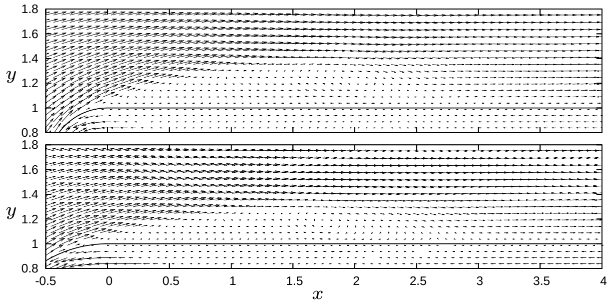

Figure 3: Velocity vectors (u, v) in $z = 0$ section for $\Lambda = 2.2$ with $\eta = 0.4$ (top) and $\eta = 0.8$ (bottom).

RESULTS

Nine simulations have been conducted by considering the combinations of η and Λ reported in table 1. For each calculation, the flow has reached a developed state after an initial period of $120H_s/U_\infty$ computed using a coarser grid followed by a transient stage of $20H_s/U_\infty$ at the current spatial resolution. All the instantaneous results presented in this paper are extracted from a subsequent temporal sequence of $20H_s/U_\infty$. Statistical data are computed using a time average over this duration. For the case $\Lambda = \infty$, statistics are also averaged in the homogeneous z-direction in order to improve the convergence level. Exactly the same inlet conditions are used for the eight simulations with inflow perturbations (the ninth calculation corresponds to a case free of inlet excitation). In practice, the constant inflow velocity U_∞ is perturbed by fluctuations corresponding to a time and spatial correlated noise (of large band-width spectrum) with an amplitude $u'_{\text{rms}} \approx 1\%U_\infty$ consistent with the residual perturbations inside the working section of the wind tunnel used by [3, 2, 4]. An important feature of these synthetic inflow fluctuations is that they have been randomly generated in the spectral space (using Fast Fourier Transform procedures) with a prescribed spectrum and a time periodicity which corresponds exactly to the duration of the final simulation, namely $20H_s/U_\infty$. For this reason, the instantaneous flows at the begin and the end of a given simulation are strongly correlated in the region highly sensitive to inflow conditions. This characteristic will be discussed in a specific section dedicated to the receptivity of the flow with respect to the inlet excitation.

Main features of the separation bubble

Here, as in the rest of the paper, we focus on the region of the flow above the body. Then, all that is discussed in the following mainly concern the dynamics near the upside of the body ($y > H_s$) without considering the motions near the edges ($z < -L/2$ or $z > L/2$). To have a complete view of the flow, the dynamics found in these lateral zones can be distinguished in some figures presented here but is not explicitly commented.

The longitudinal expansion of the separation bubble can be considered through the reattachment length l_r that corresponds to the maximum of the x-location where the time-averaged mean flow reattaches. By doing this, we use the same definition than [3, 2, 4] that did not take the separation location (occurring nearly just upstream from the end of the body curvature $x = 0$) into account to measure l_r. For flow configurations with finite Λ, this maximum value is found in the plane of symmetry $z = 0$ while for $\Lambda = \infty$, due to the homogeneous character of the flow in z-direction, l_r can be deduced in any z. Two examples of separation bubble viewed

Table 1: Reattachment length l_r and distance d_f between separation foci for each case. The values between brackets correspond to the DNS performed without inflow perturbations. Experimental measurements are from [3, 2, 4]

Λ	2.2		4.4		8.8		∞	
η	0.4	0.8	0.4	0.8	0.4	0.8	0.4	0.8
h_r	0.31	0.25(0.30)	0.36	0.26	0.35	0.21	0.25	0.18
l_r	2.7	2.7(3.4)	3.3	3.2	3.6	3.4	3.1	3.2
Exp.	2.9	2.8	–	3.4	–	3.9	–	–
d_f	2.4	2.1(2.1)	4.6	4.5	10.1	9.4	–	–
d_f/l_r	0.88	0.76(0.62)	1.38	1.41	2.80	2.75	–	–
Exp.	–	0.62	–	1.2	–	2.1	–	–

in the section $z = 0$ are presented in figure 3. The values of l_r obtained in each case are given in table 1. A good agreement is found with [3, 2, 4] for the four flow configurations reported by these authors. The strongest discrepancy concerns a case with $\Lambda = 8.8$ where it can be expected that the present use of free-slip boundary conditions at $z = \pm L_z/2$ is not realistic enough compared with the no-slip side walls of the wind tunnel used by [3, 2, 4]. Here, the side walls are located at a short distance of $(L_z - L)/2 = 0.63H_s$ from the edges of the body, so that their different effects, depending on their free-slip (DNS) or no-slip (experiments) nature, can significantly influence the dynamics in the near-body region. Despite this reservation, an interesting point is the present increase of l_r with Λ consistently with experiments. However, for $\Lambda = \infty$ (where no experiment is reported), a slight decrease can be observed by comparison with $\Lambda = 8.8$. We interpret this behaviour as a consequence of the blockage ratios which are 27:1, 14:1, 7:1 and 5:1 for $\Lambda = 2.2, 4.4, 8.8, \infty$ respectively. For the case $\Lambda = \infty$ and $\eta = 0.8$, very close to the body geometry of [9], we also attribute the lower value obtained here ($l_r = 3.3H_s$) by comparison with [9] ($l_r = 5.2H_s$) to the difference of the blockage ratios (5:1 in this work and 16:1 in the LES study of [9]). The effects of η on l_r seems to be rather limited, with a more marked influence on the shape of the separation bubble through its height h_r that is higher at $\eta = 0.4$ than at $\eta = 0.8$ for all the cases considered here (see table 1). An example of this effect can be seen in figure 3 where the increase of the height bubble is found to be mainly related to the increase of the separation angle. Once again, due to the blockage effect that depends on Λ, it is not possible to establish a clear influence of Λ on the height h_r.

The structure of the separation bubble can be characterised by the analysis of the skin-friction lines on the surface. Here, we present in figure 4 the velocity vectors in the neighbourhood of the top of the body with $\eta = 0.8$ and $\Lambda = 2.2$. For this case, the flow pattern immediately adjacent to the surface reveals the presence of six singular points. At the centre $z = 0$ of the separation line, one saddle point can be identified. Slightly further downstream, to close the separation line near each edge of the body, two foci of separation are clearly observed. Finally, one nodal attachment point located between two saddle points ends the bubble. This surface flow pattern, corresponding to a stable configuration as described by [7], corresponds very well to the measurements of [3, 2, 4] who identified the same type of surface flow topology. A quantitative comparison between present DNS and previous experimental results is proposed in table 1 where the distance d_f between the two separation foci is considered. Naturally, for the cases $\Lambda = \infty$, the separation is 2D so that only two separation and reattachment lines can be found. For the other cases, the structure of the surface flow is qualitatively similar near the separation (one saddle plus two foci points) but further downstream, the lack of convergence (the time average is only based on $20H_s/U$) does not allow us to identify clearly the singular points near the reattachment. Only the case $\eta = 0.8$ and $\Lambda = 4.4$ shows clearly the same combination of singular points than the one presented in figure 4.

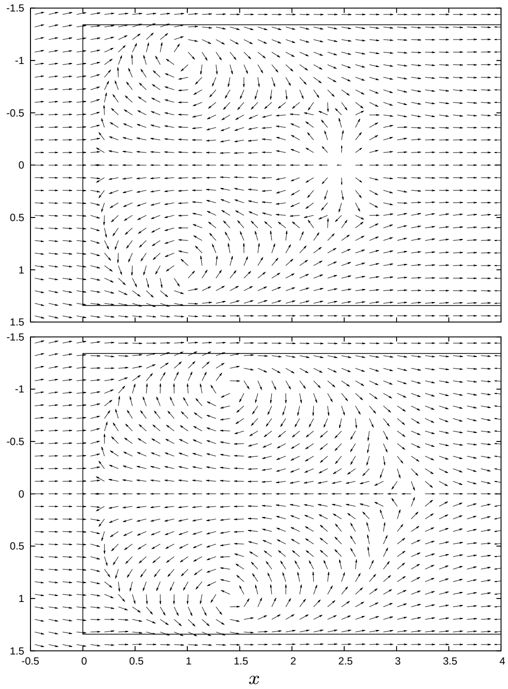

Figure 4: Velocity vectors (u, w) in the plane $y = 1.06H_s$ for $\Lambda = 2.2$ and $\eta = 0.8$ with (top) and without (bottom) inflow perturbations.

Mean flow behind the reattachment

The analysis of the mean velocity field shows that behind the separation bubble, in agreement with the usual description of 3D separated/reattached flows, the mean flow remains highly 3D with the presence of a counter-rotating pair of longitudinal vortices that tend to pump fluid from the sides toward the plane $z = 0$ where the fluid is ejected toward the top of the domain. These two mean longitudinal vortices cannot be detected using classical criteria for vortex identification. This is due to their very large scale component that is not well captured by an identification scheme based on velocity derivatives (like vorticity or the Q quantity). For this reason, we directly plot the velocity vectors in a (z, y) section downstream from the separation bubble. Because for $\Lambda = 8.8$ we cannot distinguish the presence of any longitudinal structure, only two cases are compared in figure 5 for $\Lambda = 2.2, 4.4$ with $\eta = 0.8$ (the corresponding cases $\eta = 0.4$ lead to similar conclusions). In this figure, the presence of two counter-rotating longitudinal vortices can be clearly observed. The location of each vortex pair is near the symmetrical plane $z = 0$ for $\Lambda = 2.2$ as well as for $\Lambda = 4.4$. The characteristic velocities induced by these structures are rather high ($w_{\max} = 10\%, 14\%\, U_\infty$ for $\Lambda = 2.2, 4.4$ respectively at the section presented in figure 5) so that an efficient pumping effect (from the sides to the top) remains present at $x/l_r = 1.5$ (the maximum values of lateral currents are found inside the separation bubble with

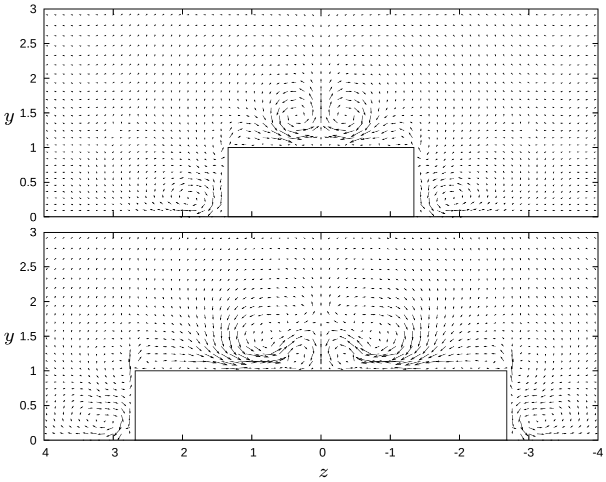

Figure 5: Velocity vectors (w, v) in $x/l_r = 1.5$ for $\eta = 0.8$ with $\Lambda = 2.2$ (top) and $\Lambda = 4.4$ (bottom).

$w_{\max} = 28\%, 36\% U_\infty$ for $\Lambda = 2.2, 4.4$ respectively). Because this analysis is only based on the mean flow, it is not possible to have an idea about the unsteady processes that are responsible from these phenomena. This point is the main subject of the next section.

Vortex dynamics

In this section, we are interested in the combined influences of Λ and η on the vortex dynamics associated with the separation and reattachment. To identify the vortical motions, we use the Q-criterion that we have found to give clearer instantaneous visualisations than vorticity for the present flow, especially in the region where instabilities are triggered. For the nine DNS presented here, we have performed the full animation of Q-visualizations using 200 velocity fields saved with a period of 0.1 H_s/U_∞. Some typical instantaneous visualisation are presented in figures 6, 7, 8, 9 and 10. As a first conclusion, the observation of the animations shows that the flow separation remains almost steady for the nine cases considered here, consistently with the experiments of [3, 2, 4]. Further downstream, the separation leads to the formation of an unstable shear layer where Kelvin-Helmholtz vortices form and roll-up through 3D processes. The frequency f associated with the formation of Kelvin-Helmholtz vortices leads to Strouhal numbers $St = fH_s/U_\infty$ consistent with the data of [3, 2, 4] (for instance, $St \approx 0.6$ here and $St = 0.58$ in experiments for $\Lambda = 2.2$ and $\eta = 0.8$). However, the present uncertainty on f (due to the limited duration of DNS) prevent us to analyse more in details St in various cases. As it can be expected, when Λ is increased, Kelvin-Helmholtz structures are found more 2D, but no significant acceleration or slowdown of primary instabilities can be noticed. Further downstream, strong distortions of primary structures occur and streamwise vortices are quickly formed by stretching. This scenario is recovered for the nine cases considered here, the appearance of 3D mechanisms being slightly favoured by a body with small Λ and somewhat inhibited by a 2D body with $\Lambda = \infty$. In the latter case, the breakdown to turbulence seems to suddenly occur near the reattachment zone. In terms of vortex dynamics, the main effect of Λ is found to be related to the shape of the typical vortical structures that develop in the separation bubble. For $\Lambda = 2.2$, a flapping of the separation bubble is observed, the resulting motion leading to a highly 3D dynamics composed of periodic eruption of

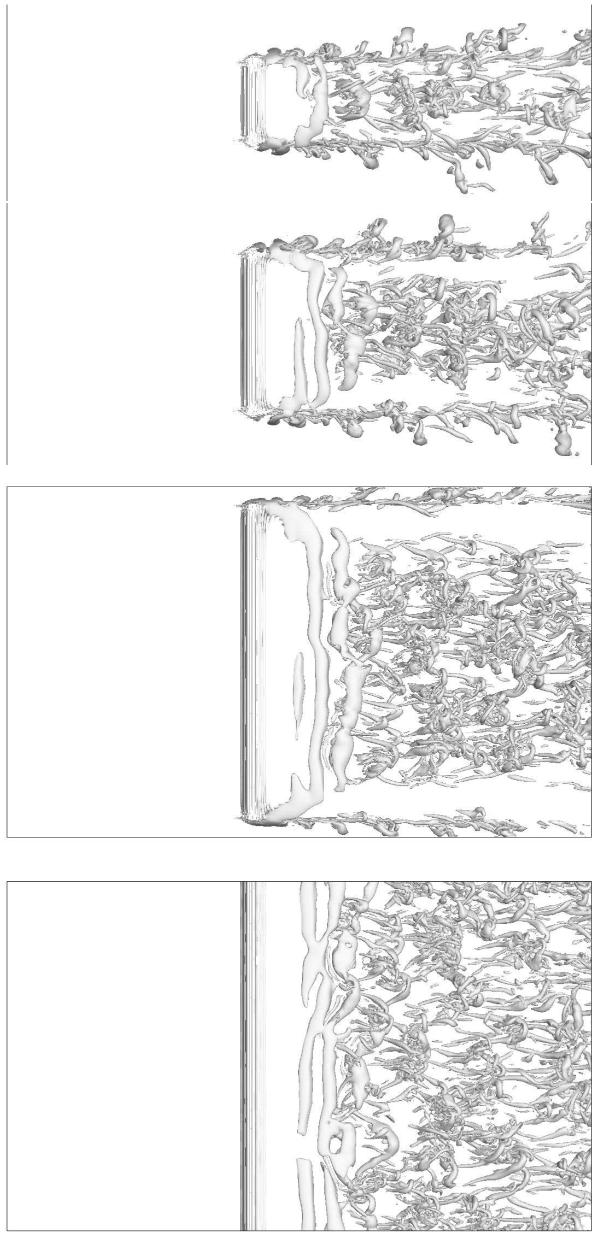

Figure 6: Top views of the isosurface $Q = 0.25$ for $\eta = 0.8$ with $\Lambda = 2.2, 4.4, 8.8, \infty$ from top to bottom (full computational domain only for the two cases with high Λ).

fluid in the middle plane $z = 0$. These phenomena are linked to the periodic formation of large scale lambda structures. The stretching by the mean flow reinforces these hairpin vortices that are also submitted to self-induction effects that tend to create strong ejection through bursting processes similar to the ones described in turbulent wall flows. These lambda structures have already been experimentally identified by [3, 2, 4] as mushroom shaped structures in cross section visualizations. For higher values of Λ, these particular large scale hairpin structures are progressively reduced and finally suppressed for the case $\Lambda = \infty$. The occurrence of marked ejections for $\Lambda = 2.2$ compared with the case $\Lambda = \infty$ can be observed in figure 7. These side views of the flow clearly show how the periodic ejections influence the growth of the boundary layer that develops over the body. Its seems reasonable to interpret the presence of the mean longitudinal vortices observed in the previous section as the

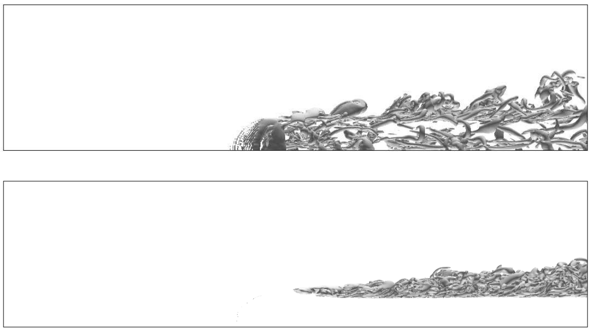

Figure 7: Side views of the isosurface $Q = 0.25$ for $\eta = 0.8$ with $\Lambda = 2.2$ (top) and $\Lambda = \infty$ (bottom).

signature of the present lambda vortices that cause central eruption of fluid alimented by a simultaneous lateral pumping of fluid from each side of the body. The reason of the creation of periodic large scale lambda vortices for the smallest aspect ratio $\Lambda = 2.2$ is probably linked to the closeness of the two foci (see table 1 to compare the distance d_f between the foci for each case) for this flow configuration. Although the connection between foci and lambda vortices cannot be directly exhibited with visualisation based on Q-criterion, we observe that large scale lambda vortices seem to emerge from the foci that can interact when the aspect ratio of the separation bubble is small enough.

The effect of the curvature of the rounded edge on vortex dynamics can be considered by comparing the top views in figures 6 ($\eta = 0.8$) and 8 ($\eta = 0.4$). Only the case $\Lambda = 8.8$ is presented here, but similar conclusions can be obtained for the other aspect ratios. Here, the main effect is that the breakdown to turbulence is significantly accelerated for the case with the strongest curvature $\eta = 0.4$. More precisely, the triggering of primary instabilities are not strongly modified by the reduction of η, but the onset of 3D secondary instabilities clearly appears before the reattachment at $\eta = 0.4$. The resulting longitudinal vortices introduce small scale motions that cause an abrupt turbulent breakdown further downstream. Comparisons between figures 6 and 8 show that smaller vortices are excited by the use of a high curvature, so that the resulting flow seem to correspond to a higher Reynolds number case. It is important to recall that the Reynolds number based on H_s is the same for both flows, while the one based on R is twice smaller at $\eta = 0.4$. To interpret the mechanisms responsible of the appearance of vortices at smaller scale, it does not seem relevant to propose a scaling with R through the definition of the Reynolds number or the direct normalisation of the typical size of the vortices. A more interesting fact, already discussed previously, is that the separation angle tends to increase with decreasing η. The resulting modification of the shape of the separation bubble is susceptible to modify its characteristics in terms of convective/absolute stability. Without considering theoretically this delicate point, the careful observation of animations in the separation bubble shows that contrary to the case $\eta = 0.8$, small structures are continuously transported from the attachment region toward the separation line by the reverse flow in the bubble for the case $\eta = 0.4$. This behaviour suggests the possibility of a self-excitation mechanism able to transmit 3D perturbations from the reattaching region to the separated shear layer and then trigger efficiently 3D secondary instabilities. This point about the downstream influence will be considered indirectly in the next section through an analysis of the receptivity of the flow to inflow conditions.

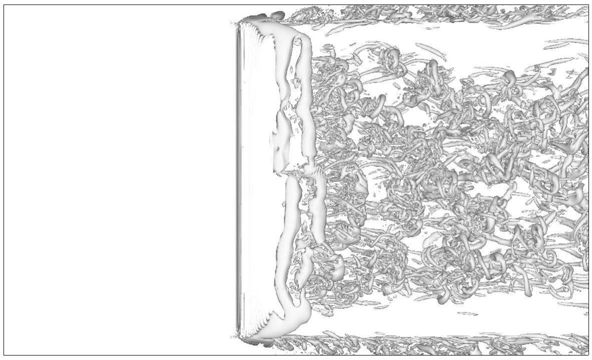

Figure 8: Top view of the isosurface $Q = 0.25$ for $\eta = 0.4$ and $\Lambda = 8.8$.

Sensitivity to inflow conditions

The question of the receptivity to upstream conditions is very delicate to address experimentally. In their experiments done in a low-speed water tunnel, [3, 2, 4] were able to reduce to 1% the level of velocity fluctuations at the inlet of the test section for the lowest Reynolds considered ($Re = 1250$) that could be obtained with $U_\infty = 0.03\,m/s$. In the present DNS methodology, it is possible to consider the same flow configuration without inflow perturbations, the residual ones corresponding to numerical errors of low amplitude. By doing this, our goal is to have a first idea about possible globally unstable nature [5, 1] of this 3D flow. At this stage of our study, we only have performed one additional simulation free from inflow perturbations by considering the case with the smallest aspect ratio $\Lambda = 2.2$ and the lowest curvature $\eta = 0.8$. The comparison of the behaviour of the flow with and without inflow perturbations can be done through the simultaneous examination of figures 6, 7 and 9. The first conclusion is that the flow remains unstable despite the lack of any excitation at the inlet of the computational domain. However, the primary instabilities are significantly delayed, so that the breakdown of the separation bubble is found to occur further downstream. This observation suggests that the shear layer in the upstream part of the separation bubble is only convectively unstable. Naturally, the increase of the steady part of the separation bubble leads to a global increase of its longitudinal size but also of its vertical expansion (rises of 30% for l_r and 20% for h_r, see table 1). Another interesting point is related to the change of the structure of the bubble depending on the presence of inflow perturbations. This can be observed by comparing the two different surface flow patterns in figure 4. For the case without inflow excitation, the set of one nodal plus two saddle points near the reattachment have been replaced by a single saddle point. Such a separation pattern is known to be structurally unstable due to the presence of a direct saddle-to-saddle connection [8, 7]. In consequence, the present use of a time average (that leads to a symmetrical surface flow) may not lead to a relevant view of the flow, the study of the unsteady component of the bubble (especially the eventual periodic motion of the foci) being required to better understand this unexpected surface flow configuration. Further downstream, the flow near the reattaching zone becomes clearly unsteady so that a breakdown can be observed with the presence of vortical structures, similar in their form to the case with inflow perturbations, but significantly less numerous. This comparative test demonstrates

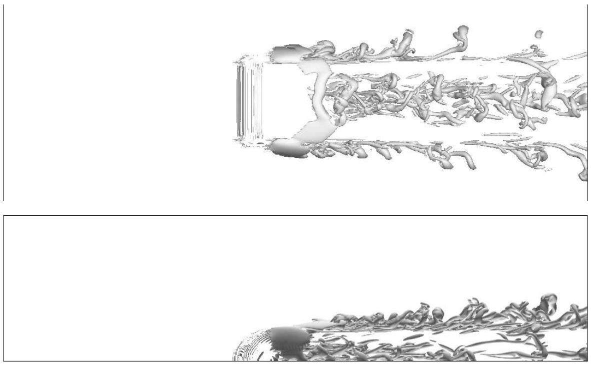

Figure 9: Top and side views of the isosurface $Q = 0.25$ for $\eta = 0.8$ and $\Lambda = 2.2$ for the DNS without inflow perturbations.

the self-excited nature of the dynamics near the reattachment region. A formal stability analysis could be interesting to interpret this behaviour in terms of convective/absolute stability, as well as additional DNS dealing with the other aspect ratios and curvature.

To evaluate the receptivity of the flow with respect to upstream conditions, another possibility consists in the comparison between two calculations based exactly on the time sequence of inflow conditions but differing from their initial state. Using the present type of inlet conditions that are purely periodic over the duration 20 H_s/U_∞ for all the DNS shown in this paper, this kind of analysis can be performed straightforwardly by comparing the initial instantaneous fields with their counterparts taken at the end of the same calculation. This principle is illustrated in figure 10 showing the initial state of the flow corresponding to its final state (20 H_s/U_∞ later) already presented in figure 6. The similarity between these two instantaneous visualisations, related to the use of strictly identical inflow excitations, can be easily observed in a significant upstream part of the computational domain. Downstream from a critical streamwise position, located in the separation bubble, the two flow realisations reveal small differences that grow continuously up to the outlet of the computational domain. Quantitatively, this behaviour can be evaluated by considering the correlation coefficient between the two flow realizations. Because present flow configuration has no direction of homogeneity for $\Lambda \neq \infty$, a rigorous computation of this correlation coefficient would need to perform a time average on a large number of fields associated pair by pair. Before performing this procedure in a further work, we preliminary have computed the correlation coefficient between the spanwise velocity component w based only on two realizations but using an average in z- and y-direction for the two cases $\Lambda = \infty$. In agreement with the simple observation of initial and final visualisations, for both cases $\eta = 0.4, 0.8$, we find that the two realisations are 100% correlated until the separation. Then, we observe two different behaviours depending on the value of η. For $\eta = 0.8$, the uncorrelation occurs slowly along x so that the two realizations remain about 80% correlated at the reattachment. For $\eta = 0.4$, immediately after the separation, a collapse of the coefficient correlation starts, with a value of about 20% in the reattached region to lead to a full uncorrelation further downstream. This drastic change in the receptivity of the flow to upstream conditions can be qualitatively recovered for other aspect ratios $\Lambda = 2.2, 4.4, 8.8$, suggesting that the nature of the stability in the separation region can differ considerably depending on the curvature.

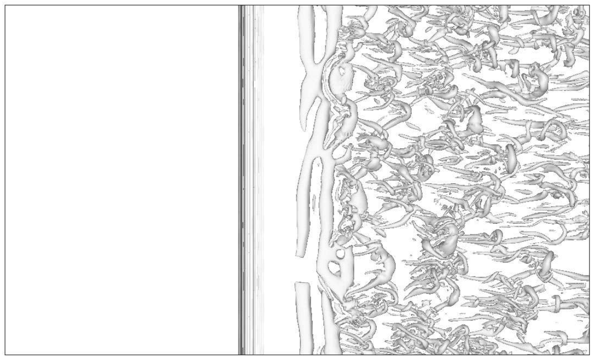

Figure 10: Top view of the isosurface $Q = 0.25$ for $\eta = 0.8$ and $\Lambda = \infty$ (initial state corresponding to the final state presented in figure 6).

ACKNOWLEDGEMENT

The simulations were carried out at the IDRIS, the computational centre of the CNRS. We are grateful to A. Spohn, S. Courtine, E. B. Camano Schettini and J.-P. Bonnet for fruitful discussions and comments on this work.

REFERENCES

[1] J.-M. Chomaz. Global instabilities in spatially developing flows: non-normality and nonlinearity. *Ann. Rev. Fluid Mech.*, **37**:357–392, 2005.

[2] S. Courtine. *Etude expérimentale des décollements provoqués par une paroi courbe : Topologie et évolution spatio-temporelle. Experimental study of flow separation on rounded front edges: Topology and spatiotemporal evolution.* PhD thesis, Université de Poitiers, 2006.

[3] S. Courtine and A. Spohn. Dynamics of separation bubbles formed on rounded edges. In *12th International Symposium on Applications of Laser Techniques to Fluid Mechanics*, Lisbon, Portugal, 2004.

[4] S. Courtine, A. Spohn, and J.-P. Bonnet. Vortex dynamics in the reattaching flow of separation bubbles with variable aspect ratio. In *Proc. of the 11th European Turbulence Conference, EUROMECH*, Porto, Portugal, 2007.

[5] P. Huerre and P. A. Monkewitz. Local and global instabilities in spatially developing flows. *Ann. Rev. Fluid Mech.*, **22**:473–537, 1990.

[6] P. Parnaudeau, E. Lamballais, D. Heitz, and J. H. Silvestrini. Combination of the immersed boundary method with compact schemes for DNS of flows in complex geometry. In *Proc. DLES-5*, Munich, 2003.

[7] A. E. Perry and M. S. Chong. A series-expansion study of the Navier-Stokes equations with applications to thee-dimensional separation patterns. *J. Fluid Mech.*, **173**:207–223, 1986.

[8] M. Tobak and D. J. Peak. Topology of three-dimensional separated flows. *Ann. Rev. Fluid Mech.*, **14**:61–85, 1982.

[9] Z. Yang and P. Voke. Large-eddy simulation of boundary-layer separation and transition at a change of surface curvature. *J. Fluid Mech.*, **439**:305–333, 2001.